HHS Public Access

Author manuscript

Nat Genet. Author manuscript; available in PMC 2019 January 23.

Published in final edited form as:

Nat Genet. 2018 September ; 50(9): 1296–1303. doi:10.1038/s41588-018-0175-z.

Dynamic interplay between enhancer-promoter topology and gene activity

Hongtao Chen[1], **Michal Levo**[1], **Lev Barinov**[2], **Miki Fujioka**[3], **James B. Jaynes**[3], and **Thomas Gregor**[1,4,5,*]

[1]Lewis-Sigler Institute for Integrative Genomics, Princeton University, Princeton, NJ 08544, USA

[2]Department of Molecular Biology, Princeton University, Princeton, NJ 08544, USA

[3]Department of Biochemistry and Molecular Biology, and the Kimmel Cancer Center, Thomas Jefferson University, Philadelphia PA 19107, USA

[4]Joseph Henry Laboratories of Physics, Princeton University, Princeton, NJ 08544, USA

[5]Department of Developmental and Stem Cell Biology, Institut Pasteur, 75015 Paris, France

Abstract

A long-standing question in gene regulation is how remote enhancers communicate with their target promoters, and specifically how chromatin topology dynamically relates to gene activation. Here, we combine genome editing and multi-color live imaging to simultaneously visualize physical enhancer–promoter interaction and transcription at the single cell level in *Drosophila* embryos. Examining transcriptional activation of a reporter by the endogenous *even-skipped* enhancers 150 kb away, we identify three distinct topological conformation states and measure their transition kinetics. We show that sustained proximity of the enhancer to its target is required for activation. Transcription in turn affects the 3D topology, as it enhances the temporal stability of the proximal conformation and is associated with further spatial compaction. Furthermore, the facilitated long-range activation results in transcriptional competition at the locus, causing corresponding developmental defects. Our approach thus offers quantitative insight into the spatial and temporal determinants of long-range gene regulation and their implications for cellular fates.

Enhancers play a key role in the control of gene expression that is essential for development[1–3]. These 50–1500 base pair *cis*-regulatory elements stimulate transcription from core promoters in a time- and tissue-specific manner by recruiting context-dependent transcriptional activators and repressors[4–6]. Whole-genome methods have shown that the

*Correspondence to: tg2@princeton.edu.

Author contributions

H.C. and T.G. conceived the main ideas regarding live cell image generation, processing and analysis. M.F. and J.B.J. developed the *homie-eve* system to create quantifiably distinct architectural and transcriptional states. H.C. designed the study to marry these technologies. H.C., M.F. and J.B.J. designed and generated the transgenic flies. H.C. and L.B. performed the imaging experiments. H.C., L.B., M.L. and T.G. analyzed the data and wrote the manuscript.

Competing financial interests

The authors declare no competing financial interests.

human genome is riddled with enhancers, with estimates ranging from 200,000 to over a million[7]. Importantly, a significant fraction of enhancers are located at large genomic distances from the promoters they regulate[8–10]. Even for a compact genome like *Drosophila melanogaster*, at least 30% of enhancer–promoter interactions occur over 20 kb, and in many cases over intervening genes[11–13].

Despite extensive studies over more than three decades, many questions still remain as to how enhancers communicate with their target promoters over large genomic distances[14]. Static measurements, employing, e.g., fluorescence *in situ* hybridization (FISH) and 3C-based genomic experiments, provided evidence supporting physical interactions between a distal enhancer and a target promoter[15–19]. Yet we still lack a dynamic characterization that could distinguish transient contact from the formation of stable topological structures and disentangle cause from consequence in the relationship between such topological structures and transcription. To address these fundamental questions we have developed a live imaging approach to track the spatial positions of an enhancer and its target promoter and to simultaneously monitor transcriptional activity in developing fly embryos. By employing this approach, we reveal, at the single-cell level, a dynamic interplay between enhancer-promoter (E-P) topology and transcriptional activity.

Live imaging of chromatin topology and transcription

To examine long-range transcriptional activation, we placed a reporter gene 142 kb from the well-studied *Drosophila even-skipped (eve)* locus, which contains a set of five enhancers that drive a seven-striped expression pattern in the cellular blastoderm (Supplementary Fig. 1). While this chosen distance is generally larger than that observed for known enhancer–promoter interactions in the early fly embryo, it is comparable to and even smaller than the distances over which many enhancers function in higher eukaryotes[8–10,20]. Notably, at such distance the chromatin fiber can display fast random movements, which creates an entropic hurdle for specific long-range chromatin interactions and thus a kinetic barrier for the establishment of a productive pre-initiation complex. We therefore included in our reporter cassette the 368bp insulator element *homie* (Supplementary Fig. 1a)[21,22], which facilitates the formation of a stable loop by self-pairing with the endogenous *homie* element[23] located at the 3′ end of the *eve* locus[21,22]. In fixed embryos containing our reporter cassette, we observe sporadic expression (~15%) of the reporter gene, solely within the limits of the endogenous *eve* stripes (Supplementary Fig. 1b), which strongly suggests that the reporter is specifically activated by the *eve* enhancers 142 kb away[21].

In order to simultaneously visualize the location of the endogenous *eve* enhancers, the location of the promoter of the reporter, and its transcriptional activity in living embryos, we designed a three-color imaging system. First, we utilized two orthogonal stem-loop-based labeling cassettes[24–26]; MS2 stem loops were introduced via CRISPR genome editing to the endogenous *eve* gene, and PP7 stem loops were added to the reporter gene (Fig. 1a, Supplementary Fig. 2a-b, Supplementary Video 1). Maternally expressed fluorescent coat proteins bind the corresponding nascent stem-loops upon transcription, providing a dynamic readout of gene activity (Fig. 1a). Owing to the strong transcriptional activity of the *eve* gene, the corresponding fluorescent focus further serves as a marker for the nuclear position

of the *eve* enhancers, which are located within 10kb of the *eve* promoter (Supplementary Fig. 1a). In addition, we took advantage of a recently developed DNA labeling system[27,28] to mark the position of the reporter gene in a manner that is independent of its activity. Namely, *Burkholderia parS* DNA sequences were included in the reporter gene, nucleating the binding of ParB-GFP fusion proteins (Fig. 1a).

Using three-color time-lapse confocal microscopy, we captured stacks of optical sections of the surface of two-hour-old (nuclear cycle 14, nc14) embryos carrying the tagged *eve* locus and the *parS-homie-evePr-PP7* reporter (Supplementary Video 2). In these stacks we can clearly identify individual fluorescent foci in 70–100 nuclei simultaneously (Fig. 1b). In the blue channel we observed the endogenous transcriptional activity of the *eve* gene in its characteristic seven-striped pattern. This pattern is quantitatively identical to that observed from the endogenous *eve* gene (Supplementary Fig. 2c-g, Supplementary Video 1). In the green channel we observed parB foci in all nuclei of the developing embryo, tracking the position and the movement of the reporter locus (Fig. 1b). Finally, in the red channel we observed the reporter's transcriptional activity in a subset of nuclei within the (blue) *eve* stripes (Fig. 1b), consistent with our results from fixed embryos (Supplementary Fig. 1b).

These three florescent foci thus provide us the means to measure the physical distance between the enhancers and the reporter, as well as to monitor the reporter's transcriptional activity. To ascertain our ability to accurately measure these properties, several control experiments were performed. To estimate the precision of our distance measurements, we generated a synthetic construct (localization control) in which all three fluorescent proteins are co-localized within a genomic distance of 2.0 kb (Supplementary Fig. 3a). By analyzing embryos carrying this construct, we were able to calibrate chromatic aberrations from the microscope and to estimate measurement errors in spot localization (180±6 nm (mean±SE), i.e. ~75nm in x/y and ~150 nm in the axial direction, see Supplementary Fig. 3b-h). Our optical resolution measured from diffraction-limited multi-color fluorescent beads is 20 nm in x/y and 50 nm in the axial direction (Supplementary Fig. 3b-h). Thus, measurement error originating from optics only accounts for ~10% of the variance in our distance measurement.

We also tested whether our genomic labeling approach introduces perturbations in the system (see experiments and discussion in Supplementary Fig. 4) by 1) removing the maternal ParB supply, 2) placing the parS sequence at different locations relative to the *lacZ* reporter, and 3) employing the more traditional lacO/LacI system instead[29,30]. In no case was the presence of ParB proteins found to affect the activation kinetics of the PP7 reporter (Supplementary Fig. 4e). Furthermore, we did not observe any significant difference in chromatin dynamics or transcription kinetics when the parS tag was placed at different locations or replaced by the lacO tag (Supplementary Fig. 4b-g). These results are consistent with previous studies, in which the parS/ParB system was found to be non-disruptive to chromatin structure[31].

An initial examination of the nuclei in which the PP7 reporter is inactive (Red-OFF) vs. those in which it is active (Red-ON) points to a close connection between transcription and the physical proximity of the enhancer-promoter (hereinafter E-P) pair (Supplementary Video 3). In Red-OFF nuclei, the reporter is well separated from the *eve* enhancers, while in

Red-ON nuclei, all three fluorescent foci appear to be attached together (Fig. 1c). Specifically, when computing the instantaneous spatial distance between the *eve* enhancer and the reporter promoter (i.e. the blue to green foci distance, E-P distance), a significantly shorter distance is observed for the Red-ON compared to the Red-OFF nuclei (Fig. 1d and Supplementary Fig. 4a-c). Moreover, computing the change in the E-P distance across a time interval of variable size gives access to the 3D mean squared displacement (MSD) for the E-P distance trajectories in the two classes of nuclei (Fig. 1e and Supplementary Fig. 4d). The MSD curve reaches a plateau for both types, indicating spatial confinement of the E-P distance. Expectedly, the size of this confinement (i.e. the spatial limit explored by the E-P pair) in the active (Red-ON) nuclei is smaller than that in the inactive (Red-OFF) nuclei (0.5^2 vs. ~1.0^2 μm^2, Fig. 1e).

Necessity of sustained physical proximity for transcription

To assess the temporal relationship between E-P proximity and the processes of transcriptional activation and inactivation, we identified all time traces in which we observed nascent transcription in the PP7 reporter gene switching from OFF to ON (n=286) and switching from ON to OFF (n=203), respectively. When we aligned ~20 min time windows of both sets of traces centered around the switching time point, we observed a strong association between physical proximity and activity.

The OFF-to-ON set (Fig. 2a, Supplementary Fig. 5a-b, Supplementary Video 4a-c) displays a sharp transition in transcriptional activity, with rates comparable to those previously reported for active nuclei exiting mitosis[32]. The distance between the *eve* enhancers and the reporter promoter (i.e., the blue to green foci distance) converged continuously until this sharp onset of transcription. At this point the E-P distance (root-mean-squared (RMS) distance) corresponds to ~340 nm. These findings suggest that E-P proximity is required in order to initiate the transgene's transcriptional activity.

Correspondingly, the sharp drop in transcriptional activity observed in the ON-to-OFF set of time traces is accompanied by an increase in the RMS E-P distance (Fig. 2b, Supplementary Fig. 5c-d, Supplementary Video 4d-f). While polymerases (RNA polymerase II, PolII) already engaged in transcription will continue to give rise to a detectable red focus even after the separation of the *eve* enhancers from the promoter (likely accounting for the largest part of the observed ~4 min delay[32,33]), it seems transcription initiation ceases as soon as the *eve* enhancers and the reporter promoter physically separate. Overall, these results fit with a model in which sustained E-P physical association is necessary for continuous initiation of transcription.

Characterization of three topological states

To establish a quantitative link between physical proximity and transcriptional activity, we constructed the distribution of time-averaged RMS E-P distances, across all data acquired. We examined time traces from 7,883 nuclei, across 84 individual embryos, taken over a 30 min period in nc14 and calculated the time-averaged RMS E-P distances over a sliding window along each trace (Fig. 3a and Supplementary Fig. 6a, see Methods). We found a bi-

modal distribution that can be fitted by a mixture of two Gaussians, one harboring 87% of all RMS samples with a mean of 709±110 nm (mean±STD) and the other, smaller in proportion, with a mean of 353±82 nm.

To gain insight into the topological conformation underlying these two disparate populations, we employed a variant of our reporter construct in which the *homie* sequence is replaced by λ DNA of the same length (*parS-λ-evePr-PP7*). When we constructed the corresponding RMS E-P distance distribution from 1,453 nuclei in 15 embryos carrying this construct, we observed a unimodal Gaussian with a mean of 730±112 nm, similar to the large population obtained with the *parS-homie-evePr-PP7* construct (Fig 3a and Supplementary Fig. 6c). This indicates that the Gaussian with the larger mean, common to both constructs, likely represents nuclei in an open, unpaired conformation. In contrast, the smaller population, with the short E-P distances, observed only with the *homie*-containing construct, likely stems from nuclei in a *homie–homie* paired conformation, which are evidently missing in the λ replacement construct. Furthermore, consistent with these postulated underlying conformations, the mean of the large Gaussian increases (i.e., shifts to larger distances) when we move the PP7 reporter to a genomic location more distal from the *eve* locus (from −142 kb to −589 kb, Supplementary Fig. 6d), while the mean of the smaller Gaussian remains unchanged. In addition, the size of the smaller Gaussian is clearly reduced in reporter constructs containing truncated versions of the *homie* element (Supplementary Fig. 7).

Using these distance distributions, we next examined reporter activities. The most noticeable observation stems from the reporter with the λ replacement, in which transcription is largely abolished. This confirms the necessity for sustained proximity for productive transcription in our system. Indeed, for the *parS-homie-evePr-PP7* construct, the sub-distribution of the E-P distances obtained only from time traces displaying PP7 transcriptional activity is fully contained within the smaller Gaussian (red curve in Fig 3a, Supplementary Fig. 6a), i.e. all transcriptionally active reporters are physically close to the *eve* enhancers. However, among all E-P distances occupying the small Gaussian, in only 54% is the reporter active (Fig 3a). The presence of traces in which the promoter is close to the enhancers but nevertheless inactive (green curves, Fig 3a, Supplementary Fig. 6e) suggests that the proximity obtained by *homie–homie* pairing is not sufficient to ensure transcription. Notably, upon *homie–homie* pairing, the linear genomic distance between the reporter promoter and the *eve* enhancers is less than 10kb, which is similar to the enhancer-promoter distances in the endogenous *eve* locus. Thus, while architectural proteins can bridge the gap between long-range enhancer-promoter interactions (e.g., 142kb) and short-range interactions (e.g., 1-10kb), the facilitated proximity is not sufficient to assure transcription.

Transcription reinforces topological compaction

Our analysis reveals three possible topological states of E-P interaction: 1) open conformations that are transcriptionally inactive (O_{off} state), 2) *homie–homie* paired conformations that are transcriptionally inactive (P_{off} state), and 3) *homie-homie* paired conformations that are transcriptionally active (P_{on} state). To assess the physical properties and the transition kinetics of these states, we assigned each time point of the 7,883 time

traces to one of the three states. Specifically, we used a Bayes classifier to distinguish between the unpaired and the paired state, using time traces from the *parS-λ-evePr-PP7* construct for the open state (O) and time traces with PP7 activity for the paired state (P) as training samples. Furthermore, we used the presence of the PP7 (red) signal to further divide the paired state (P) into an inactive P_{off} state and an active P_{on} state (Supplementary Fig. 8a-j; for detail see Methods).

When we compared the distance distribution of the inactive paired (P_{off}) and the active paired (P_{on}) states, we found that the mean (±STD) RMS E-P distance for the P_{off} state (385±15 nm) is significantly larger than for the P_{on} state (331±16 nm) (Fig. 3d and Supplementary Fig. 8k). The shorter RMS distance in the transcriptionally active state is indicative of an enhanced compaction of the locus when the reporter is active.

To further examine the relationship between compaction and transcription, we employed an additional variant of our reporter cassette, in which we deleted the promoter from our transgene (*parS-homie-noPr-PP7*). The RMS E-P distance distribution for this construct recovers the bi-modal distribution from the original construct representing the O_{off} and P_{off} states (calculated from 2,566 nuclei in 29 embryos, Fig. 3a and Supplementary Fig. 6b). In particular, the mean RMS E-P distance of the P_{off} state measured for this promoter-less construct (374±14 nm, mean±STD) coincides with that measured for the full construct (Fig. 3c, Supplementary Fig. 8k), and is thus larger than that of the P_{on} population (Fig. 3d, Supplementary Fig. 8k). Together, these results argue for the association of transcription with a smaller physical confinement.

Transcription enhances stability of the paired conformation

Interestingly, we found that the *parS-homie-noPr-PP7* construct, which is non-permissive for transcription, has a smaller fraction of the population in the *homie* paired conformation (P state) than does the *parS-homie-evePr-PP7* construct, which is permissive for transcription (8% versus 13%, Fig. 3c-d). This suggests that transcription is not only associated with a more confined spatial conformation but may also be associated with a temporal stabilization of the paired conformation.

In order to test this, we use a set of first-order reactions to model the kinetic transitions between the three topological states described above (Fig. 3e, Supplementary Fig. 9a, see Methods). Using this model, we determined the transition rates by fitting the model-derived equations to the measured time courses of the fractional occupancies for each of the three states (Fig. 3e and Supplementary Fig. 9a-h). The transition from an open topology to the *homie-homie* pairing state ($f_1 = 0.017\ min^{-1}$) takes on average 1h. This rate is ~8 times slower than the time it takes for the enhancer to explore the entire confined space in the vicinity of the promoter in the *parS-λ-evePr-PP7* construct, as predicted by our MSD results, assuming a simple first-passage model[34] (where the time $t=(1.1\mu m^2/6D)^{1/\alpha}$, Fig. 1e and Supplementary Fig. 4d). It is possible that the *homie* orientation preference for pairing[23] (as was also described for other architectural factors, such as CTCF[35,36]) constrains productive passages, thereby contributing to this slower rate. Notably, this rate of pairing is roughly an order of magnitude slower than the rapid transcriptional events that take place in the early

fly embryo. This requirement of rapidity is possibly facilitated by closer E-P distances, characteristic of early developmental genes, than the 142kb that we explored here.

Examining the other transition rates obtained from our model confirms the stabilizing effect of transcription on locus topology: the dissociation of the *homie–homie* pairing complex in the absence of transcription ($b_1 = 0.144\ min^{-1}$) is on average over ten times faster than the escape from the transcriptionally active state P_{on} ($b_2 = 0.014\ min^{-1}$, $b_3 = 0.011\ min^{-1}$, Supplementary Fig. 9e-g). These rates capture the escape from the transcriptionally active state P_{on} (b_2 and b_3) and recapitulate quantitatively the measured durations of transcriptional activity (length of Red-ON trajectories, Supplementary Fig. 9h). Intriguingly, the average duration of the transcriptionally active state is about 40 min ($1/(b_2+b_3)$), which coincides with the length of the developmental time window in which the *eve* stripe enhancers are active in nc14. This transcription-dependent stabilization might thus serve to reinforce the locus functionality for the appropriate developmental time scales.

Ectopic E-P interaction results in developmental defects

In our experiments, the *eve* stripe enhancers, distributed within the ~16kb of the *eve* locus (Supplementary Fig. 1a), drive expression of both the introduced reporter gene and the endogenous *eve* gene, which could possibly lead to competitive dynamics. To test this hypothesis, we compared *eve* transcriptional activity (i.e., the intensity of the blue MS2 signal) in each individual nucleus in which the PP7 reporter gene is active to the activity in its neighboring nuclei in which the reporter is inactive (Fig. 4a, see Methods). Strikingly, for each *eve* stripe, we measured a 5%-20% reduction in endogenous *eve* transcription in nuclei in which the reporter gene is also transcribed compared to neighboring nuclei in which it is not transcribed. The average reduction per nucleus is highest for stripe 5, and lowest for stripes 3 and 7.

eve is a primary pair-rule gene that is essential for segment patterning, allowing us to test whether the observed reduction in *eve* transcription has a phenotypic consequence. We crossed males carrying a tag-less *homie-evePr-lacZ* transgene at −142 kb to females heterozygous for a wild-type *eve* gene and an *eve* deficiency (Df(2R)*eve*) (Supplementary Fig. 10a). *eve* is weakly haploinsufficient, and 6% of +/*Df(2R)eve* flies display patterning defects in even-numbered parasegments (Supplementary Fig. 10b-e). Consistent with the reduction in the level of *eve* nascent transcripts, the presence of the *homie-evePr-lacZ* transgene exacerbates *eve* haploinsufficiency (Fig. 4b-d, Supplementary Fig. 10a). Altogether 27% of the *homie-evePr-lacZ/Df(2R)eve* flies have abdominal defects, which corresponds to a ~5-fold increase compared to the control crosses in which *homie* is replaced by phage λ DNA (Fig. 4e, Supplementary Fig. 10a). Taken together, these results suggest that interference between two promoters in the early embryo can have phenotypic consequences for patterning in the adult. These findings reinforce the view that manipulating topological chromatin structures can functionally alter developmental programs[37,38].

Discussion

Simultaneous multi-color live imaging of gene activity and the positions of genomic foci reveals a dynamic interplay between chromatin topology and transcriptional activity. By analyzing this interplay, we identify a requirement for a distinct topological structure that brings promoter and distant enhancer together in the nucleus, formed through pairing of insulator elements, for the initiation and maintenance of transcription. The temporal concordance between cessation of transcription and physical dissociation of this paired conformation argues against a suggested 'hit-and-run' model and argues in favor of the requirement for persistent physical E-P proximity for sustained transcription.

Notably, the physical proximity attained by insulator pairing is not a guarantee for transcriptional activation. This observation will prompt further investigation as to the mechanisms underling the transition to an active state. These might involve a second, entropy-based search step resulting in direct physical contact between the enhancer and promoter, and/or entail transcription factor binding with the involvement of other components of the transcription machinery (e.g., mediator, PolII pause-release), or a change in local chromatin accessibility, each of which was previously associated with transitions from a transcriptionally 'off' to an 'on' state[12,39–43].

Our measurements provide further insights into the open debate whether topology precedes transcription[44,45]. Specifically, our results argue for a complex interplay, as we observe a transcription-mediated reshaping of the kinetic landscape of 3D genome organization. While transcription requires physical proximity, it is in turn associated with further spatial compaction and temporal stabilization. It is possible that transcription can only occur within close proximity (even within the range of P_{off} distances), and that the observed spatial compaction could result from a biased sampling of the P_{off} distribution by transcription and not necessarily an active mechanism of compaction. The observed compaction is also consistent with recently proposed hypotheses that phase behaviors might contribute to the formation of Pol II 'factories' or transcription 'hubs' within topologically associated domains[46–48].

Overall, we identify and characterize three states; one in which the distal enhancer and the promoter are not together (O_{off}), a second in which they are "within range" (as afforded by insulator pairing) but the gene is transcriptionally inactive (P_{off}) and a third, which seems stabilized by transcriptional activation (P_{on}), and in which they are close together. These results are consistent with several recent observations obtained from fixed samples, including observations of proximity of an enhancer to a promoter prior to activation[12], and of an increase in co-localization in expressing tissues[49]. Our observations suggesting that transcription is associated with a different 3D landscape are also in line with recent Hi-C experiments carried out in the early *Drosophila* embryo, in which the authors suggest an effect of transcription on local chromatin organization, such as co-localization of boundaries and local compaction[44].

Interestingly, topological domain boundaries, as captured by recent early embryo Hi-C experiments, coincide with DNA regions that are rich in insulator protein binding[44,50].

Indeed, previous studies showed that insulator proteins demarcate regulatory units of the fly genome, often separating differentially expressed genes[51]. These proteins have been suggested not only to contribute to the formation of boundaries but also to facilitate physical interactions between boundaries to form "loop domains"[44,50], likely through protein pairing[52]. Importantly such interactions between insulators were specifically also implicated in mediating long-range activation[52,53]. While such long-range interactions might not be ubiquitous in the very early embryo undergoing rapid nuclear divisions (0-2 h), in slightly older embryos (3-8 h) they were found to be prevalent (with a reporter median distance of 110 kb)[12].

Our observation of a nearly inactive reporter at a distance of ~140 kb in the absence of the *homie* insulator suggests the necessity of these architectural elements in mediating long-range activation. Naturally, the exact properties of such elements could differ, affecting for instance the likelihood of pairing even upon an encounter (e.g. depending on orientation preferences) and the stability of the paired configuration. Such differences could then influence to some degree the kinetics of transcription (e.g. affecting the rate of escape from the paired transcribing state). In the constructs presented here we chose to include the *homie* element, due a documented role in the endogenous *eve* locus[22]. This allowed us to obtain pairing over long distances and thereby enabled our live examination of enhancer-promoter interactions, linking 3D topology and transcription. The overall landscape of the fly genome, as it emerges from mapping insulator binding, chromosome conformation capture experiments, and locus-specific studies, suggests that our genomic constructs (with activation over >100kb distance, and with physical proximity facilitated by insulator pairing) are capturing fundamental properties of long-range activation in flies, and likely also in other higher eukaryotes.

Finally, we show that a perturbation involving long-range activation by an endogenous enhancer can have clear phenotypic implications. This strengthens previous observations linking disease and aberrant transcription to 3D genome structure[38,54], and highlights the necessity of methods to mechanistically study these links[55]. Extensions of our approach to study different genes, regulated by enhancers at different distances, whose interaction is mediated by different architectural proteins, and in various developmental stages and organisms, will thus likely uncover new mechanistic insights into enhancer–promoter interactions.

Online Methods

Plasmid construction

The MS2 stem loop cassette is amplified from a previously described *hb*P2-MS2 plasmid[32]. An optimized 24×PP7 sequence is a gift from T. Fukaya[26]. *homie* is amplified from chr2R: 9,988,750-9,989,118 (dm6). parS sequence from *Burkholderia* (J2315, chr3:3,440-3,821, GB: AM747722) is a gift from K. Bystricky and F. Paire. MCP and PCP are amplified from Addgene #52985[56]. 3xmTagBFP2 is amplified from Addgene #62449[57]. mKate2 is a gift from J. Ling, and a set of three was fused to make 3xmKate2. ParB-GFP is a gift from K. Bystricky and F. Paire. The 256xlacO cassette is cut from addgene #33143[58]. LacI::GFP is amplified from Addgene #40943[59]. All plasmids used for transgenic experiments were made

through standard cloning procedures. Plasmid maps and cloning details are available upon request.

Transgenic fly generation

To tag endogenous *eve* with MS2 stem loops, a two-step transgenic strategy was used. First, an attP site was integrated into the 1st intron of *eve* using CRIPSR-mediated homology-directed repair. The homology arms were amplified from the genomic DNA of BDSC #51324, which was used as a genomic source for *nos*-Cas9. The two Cas9 cutting sites are at chr2R:9,979,604-9,979,605 and chr2R:9,980,605-9,980,606 (dm6), respectively. Second, an attB-MS2-lacZ-eve3′UTR plasmid was used to deliver MS2 into the attP site. A genomic source of phiC31 integrase (BDSC #34770) was used for the second injection. The final *eve*-MS2 transformant carries a ~9.5kb insertion (selection markers) between the *MS2-lacZ-eve* 3′UTR and the downstream *eve* enhancers.

The *eve-MS2* flies were crossed with a 2xattP genomic landing site at chr2R:9,836,454 (dm6, −142kb to *eve* promoter[22]) to obtain recombinants that carry *eve-MS2* and the −142kb landing site in *cis*. The reporter transgenes were then integrated into the landing site through recombination-mediated cassette exchange using BDSC #34770 as the integrase source.

For the fluorescence-tagged maternal proteins (MCP::3xmTagBFP2, PCP::3xmKate2 and MCP::mCherry), a genomic landing site at 38F1[60] was used. For maternal ParB::eGFP, LacI::GFP and PCP::eGFP, a landing site at 89B8 was used. All microinjections were performed as described previously[61] or through *BestGene* injection service.

Fluorescence in-situ hybridization

smFISH followed a previously described protocol[62]. Atto labeled probe sets targeting *eve* CDS and the 5′ 1.7kb of *lacZ* were used. Raw images were processed following Little et al. [63] to identify all cytoplasmic spots and transcription spots. A cytoplasmic unit (CU) that corresponds to the fluorescence intensity of a single cytoplasmic mRNA was calculated. Specifically, a sliding window of 220×220×23 pixel (16.5×16.5×7.4 μm^3) was applied to the raw image stack and the total pixel values in the window were plot against the number of cytoplasmic spots found in the window. A linear fit in the range of 0-100 cytoplasmic spots was applied to extract CU for each probe set (Supplementary Fig. 2f, inset). In order to get the number of Pol II in each transcription spot, a cylinder mask (d=13 pixel, h=7 pixel) centered at the brightest pixel in each transcription spot was used to calculate total spot intensities, which were converted using the corresponding CU and probe configuration for the transcribed sequence. Because the *eve-MS2* allele is targeted by only a part of the *eve* probe set, a conversion factor was calculated from the proportion of bound probes. The CU obtained from the full-length *eve* transcripts was then adjusted using this conversion factor in order to get pol II number on *eve-MS2* from the *eve* channel (y-axis in Supplementary Fig. 2f).

Phenotypic scoring

The *homie-evePr-lacZ/CyO* flies or the *λ-evePr-lacZ/CyO* flies were crossed with an isogenic *yw;Sp/CyO* (BDSC #8379) to get *Sp/homie-evePr-lacZ* and *Sp/λ-evePr-lacZ*

males. Single males were then crossed with *CyO/Dp(2R)eve*$^{-}$ virgins[22] in order to score phenotypic defects in the next generation. Since phenotypic penetrance can be very sensitive to environmental conditions (e.g., temperature, humidity, food, etc.) and genetic background, our crossing and scoring scheme included controls for all these potentially confounding factors.

Microscopy and imaging conditions

For imaging parS containing transgenes, virgins carrying three fluorescent protein fusions (*yw*; MCP::3xmTagBFP2/PCP::3xmKate2; ParB::eGFP/+) were crossed with males carrying the *eve-MS2* allele and the reporter transgene. For the 0kb co-localization control, virgins carrying three fluorescent protein fusions (*yw*, MCP::3xmTagBFP2/MCP::mCherry; PCP::eGFP/+) were crossed with males carrying the hbP2-24×MS2PP7-*kni* transgene. For the lacO/LacI control, virgins with three fluorescent protein fusions (*yw*; MCP::3xmTagBFP2/PCP::3xmKate2; LacI::GFP/+) were used. The embryos from the above crosses were manually dechorionated and mounted as described[32]. For bead experiments, 200 nm three-color coated TetraSpec beads were used.

All images were acquired on a Leica SP5 confocal microscope with a Leica oil immersion 63× NA1.44 objective. Three laser lines at 405 nm (0.4 μW), 488 nm (1.1 μW) and 591 nm (0.5 μW) were used to excite the blue, green and red fluorophores, respectively. For bead experiments, we modulated laser powers in order to get a spectrum of emission signals. Three HyD detectors in photon counting mode were used to collect fluorescence emission spectra. Voxel size for all images was set at 107nmx107nmx334nm, and the total volume imaged was about 110×27×8 μm^3. Frame interval for all time-lapse videos was 30 s, except for the ones shown in Fig. 1C (15 s). Images were taken at 1,024×256×25 voxels and focused on the posterior half of the embryo, encompassing *eve* stripes 3–7. Embryos that exit mitosis 13 were timed[64]. Imaging started at 20±2 min into nc14 and finished at gastrulation (62±2 min into nc14).

Image processing and data analysis (All image processing and data analysis was performed using MATLAB R2015a, MathWorks):

1. Nuclear segmentation and tracking—Nuclear segmentation was performed on the difference between the blue and red channels (NLS::MCP::3xmTagBFP2 is enriched in the nuclear compartment while ParB-eGFP is enriched in the cytoplasm): the maximum z-projection of the green channel was subtracted from the blue channel, and the resulting image was subsequently Gaussian blurred (σ=5), binarized (using a local Otsu's threshold at 5×5 μm^2) and opened with a disk of diameter d=5 pixels. A watershed transformation was performed on the distance matrix calculated from the binarized image to get the segmentation for each frame, and a nuclear mask was calculated from each segmented region.

Since each frame contains only 70–100 nuclei, we used an exhaustive search for nuclear tracking. Because both the whole embryo and the nuclei might move during imaging, we calculated a local vector that recapitulates the nuclear movement by minimizing cross-correlation between nuclear masks of two consecutive frames. After correcting for

movement, we multiplied each nuclear mask at time *t* to all individual nuclear masks from *t* +1, and the matching nucleus was selected based on the total pixel value of the product images. All nuclear segmentation and tracking results were scrutinized manually.

2. Candidate spot identification—We build a candidate spot library for each video. First, raw image stacks from each of the three channels were sharpened using a 3D bandpass filter of size 11×11×7 pixels, which was derived from subtracting a uniform filter from a Gaussian kernel (σ=(1, 1, 0.6) pixel). We treated all local maxima in the filtered image as putative spots, and a cylinder mask with diameter of 13 pixels (1.4 μm) and a height of 7 pixel (2.3 μm) centered at each local maximum was constructed. The size of the mask was determined by the size of the mega-spot images (Supplementary Fig. 3e-h) and covered >97% of signals emitted from the chromatin foci. Therein we summed up all pixels inside the mask to get the intensity of each putative spot. Finally, for each nucleus at each time point, an intensity threshold was chosen to select candidate spots from the local maxima, in such a way that the maximum number of candidate spots in the nucleus was less than 20. In the subsequent steps, we filtered the candidate spot library using information on nuclear lineage, spot tracking and the relative location of spot pairs.

3. Spot tracking—The intensity-weighted centroid was calculated within the mask of each candidate spot, and the *FracShift* algorithm[65] was applied to find the sub-pixel center for each spot. No sub-pixel bias was observed after 10 *FracShift* iterations. We did spot tracking in each nuclear lineage. For each lineage, candidate spots located in the corresponding nuclear region (from the nuclear segmentation results) were used for tracking. Spot tracking was performed in three steps: a pre-tracking step, a gap-filling step and a Bayes filtering step.

Step I: For the pre-tracking step, we tracked the two brightest candidate spots in each nucleus. The maximally allowable displacement of spots from the consecutive frames was determined from the MSD at $\Delta t=30s$ (1 frame, see Part 9 below and Supplementary Fig. 4d) and the measurement error (e_L, see Part 5 below and Supplementary Fig. 3a-d) for each dimension. Specifically, for each candidate spot at time t, a search zone of size 3× ($\sqrt{\mathrm{MSD}/2}+e_L$) was set up around the spot center. After correcting for nuclear shift, a candidate spot in the searching zone at time $t+1$ was recorded, and other candidate spots were discarded. In the <1% of cases where there was more than one candidate spot in the search zone, the brightest one was chosen. Finally, all traces shorter than 2 min are treated as false positives and discarded. These false positive traces are usually clusters of completed mRNAs that are undergoing nuclear export. All tracking was performed on videos of 35 min length (22–58 min in n.c.14). The three channels (MS2, PP7 and parS) were tracked independently. Pre-tracking results from all channels were compiled according to nuclear lineages.

Step II: After collecting the pre-tracking results, we analyzed for each channel 1) the distribution of spot axial positions, 2) the distribution of spot intensities, 3) the distribution of displacement vectors, and additionally for the blue (*eve-MS2*) channel, 4) the distribution of spot anterior-posterior positions. We then implemented a Dijkstra algorithm[66] to find the minimal path that fills the gaps in the pre-tracking results. Specifically, using the distributions described above, we calculated a cost function (log likelihood) for each link

that connects any two candidate spots from two consecutive frames, and constructed the set of links that minimized the sum of the costs across the gap. At the end of this gap-filling step, we obtain one tracked spot for each nucleus at each time point.

Step III: Finally, we filtered these tracked spots using a Bayes binary filter. First, a false positive data set (FP) is constructed by re-tracking the candidate spot library after removing spots that were previously tracked. The pre-tracking result from Step I was used as the true positive set (TP). For each spot obtained from Step II, we then used the information (info) of its location, intensity, the displacement from the previous frame and the displacement toward the next frame to obtain likelihood p(info|FP) and p(info|TP), respectively. Next, we calculated the priors p(FP) and p(TP) by fitting a two-component Gaussian mixture model for the vectors that connects the tracked blue and green spots in the same nucleus. Finally, we obtained the posterior probability p(TP|info) and used a cutoff that maximizes the Matthews correlation coefficient to filter false positive spots. The sensitivity of the filter ranged from 96.2% to 99.1%, and the false discovery rate was less than 1%.

4. Calibrating chromatic aberrations—Chromatic aberration was corrected in order to measure distance between spots of different colors. The calibration was data-driven and internally controlled. We assumed that the vector between a spot pair of two different colors in the same nucleus has a zero mean in each dimension. An MS2 spot (blue), for instance, has the same probability of appearing on top of the associating parS spot (green) as the probability of appearing below it, and the distribution is symmetric around zero. We performed additional control experiments to verify this assumption (see below).

We pooled raw instantaneous spot-pair distances from all nuclei at all time points in all available embryos and analyzed the raw distances as a function of the spot-pair positions in the image field of view (e.g., Supplementary Fig. 3b shows the blue-green distance in the x-direction as a function of the x-position in the image of view). We applied a multivariate normal regression model ($A_i = p_i\beta + e_i$, i=x,y,z) in order to get the correction matrix β, where A_i is the 3-D response vector for the chromatic aberration, p_i is the spot position with a constant term and e_i is a normally distributed error. For each spot pair, chromatic aberration was calculated using β, and the calibrated distances were used in further analysis. The correction matrix was calculated on a weekly basis, using all embryos imaged over the week (embryo number ranging from 12 to 25, usually of the same genotype).

In order to test the validity of the zero mean assumption described above, we did two control experiments. First, we imaged our co-localization control embryos in which blue, green and red fluorescent proteins co-localized within a genomic distance of 2 kb (Supplementary Fig. 3a). Second, we made videos of the 200 nm 3-color *TetraSpec* beads. These experiments were performed during the same week and under the same optical settings as for the *parS-homie-evePr-PP7* embryos, and the images were analyzed using the same code pipeline. Next, we applied the same calibration method to obtain the correction matrix for the control embryos or beads. There was no significant difference between the fitting parameters obtained from the *parS-homie-evePr-PP7* embryos and those from the control embryos or beads (Supplementary Fig. 3b). Specifically, applying the correction matrix derived from the

control embryos on the experimental embryos introduced <0.6% difference in the calibrated distances.

5. Estimating localization errors—In order to estimate the precision in our distance measurement, we used the 3-color control embryos described above. Briefly, the standard deviation (STD) from the fitted line (Supplementary Fig. 3b, middle), which is the mean after chromatic correction, represents the localization error (e_L). For example, for the distance between the MS2 (blue) and parS (green) spots, the STDs for the lateral and axial direction are 75 nm and 150 nm, respectively (Supplementary Fig. 3c). These errors were subtracted in the calculations of time or population-averaged RMS distances (see Part 6 below).

We then assessed whether these localization errors result from optics or from the dynamic properties of our live embryos. From the beads videos we measured lateral and axial errors of 20 nm and 50 nm, respectively (Supplementary Fig. 3c). The differences in the measurement errors between embryos and beads were not due to differences in photon counts (Supplementary Fig. 3d). We conclude that approximately 2/3 of our localization errors were derived from the properties of the live system. At least two factors might contribute to the increased errors we observed in the embryo. First, the nuclei were imaged during S or G2 phase, and individual transcription spots actually represent two sister chromatids. Second, each z-slice takes ~1 s, and the expected MSD is ~0.1 μm^2 from the extrapolation of our MSD analysis. As a result, the movement of the spots between two consecutive z-stacks introduces ‘motion blurr’, which leads to increased localization error. Since the *parS-homie-eve-PP7* embryos are expected to share the same biological and optical properties as the 3-color control embryos, we assume the same localization errors.

6. Calculating RMS (root-mean-squared) distances—We report time- or population-averaged RMS distances between the MS2 (blue) and the parS (green) spot pairs. For time-averaged RMS distances, instantaneous distances measured at different time points in the same nucleus were averaged. We analyzed the distribution of RMS distances calculated at different time scales, either for the complete time trace (Supplementary Fig. 6) or for a short time window (5 min, Fig. 3a) in order to characterize topological transitions occurring at the relevant time scales. We further classified all RMS distances into two groups (Red-ON and Red-OFF) according to the presence or absence of the red signal (*PP7* transcription). For RMS distances obtained from the complete traces, Red-OFF RMS distances were calculated from traces that never show PP7 transcription, while Red-ON RMS distances were calculated from the part of the traces that displayed PP7 activity (Supplementary Fig. 6). For RMS distances obtained from short sliding time windows, Red-OFF RMS distances were calculated from traces that never showed PP7 transcription, and Red-ON RMS distances were calculated from traces that displayed PP7 activity at all time points across the window (Fig. 3a).

We also calculated population-averaged RMS distances (Fig. 2, Fig. 3b-d and Supplementary Fig. 8k) for a group of nuclei that shared the same temporal or spatial register. For example, we aligned all traces with Red-OFF to Red-ON transitions and calculated the RMS distances from nuclei aligned at the same time relative to the initiation

of PP7 transcription (Fig. 2a). Similarly, we calculated RMS distances for all nuclei classified as being in the same topological state (Fig. 3b-d and Supplementary Fig. 8k).

Since the measurement errors (e_i) described in the previous section and spot pair distances did not seem to be correlated, we reported an error-corrected RMS_{corr}, obtained by subtracting the errors from the raw RMS distances: $RMS_{corr}^2 = RMS^2 - \Sigma_{i=(dx,dy,dz)} e_i^2 = \Sigma_{i=(dx,dy,dz)} <i+e_i>^2 - \Sigma_{i=(dx,dy,dz)} e_i^2$, where i is the actual blue-green (MS2-parS) distance in each dimension and e_i is the localization error in the corresponding dimension, which is the STD obtained from the 3-color control (Supplementary Fig. 3c).

7. Gaussian mixture fits—The PDFs (probability distribution functions) of RMS distances (except for the λ control in Fig. 3c) were modeled with two-component Gaussian mixtures with five parameters: two means (μ_1 and μ_2) and STDs (σ_1 and σ_2) for the two Gaussians and the proportion (p) of the components. Maximum likelihood estimates were performed using MATLAB's *mle* function. The fitting results were robust to the choice of initial values, and convergence was always reached after 250 iterations. For the *parS-homie-evePr-PP7* embryos, the Gaussian component with the smaller mean is composed of two populations.

8. Time trace alignment—Time series of *PP7* activities were aligned with respect to 1) the initiation of *PP7* transcription, i.e. the first time point at which nascent *PP7* transcripts (red spots) could be detected, or 2) the termination of *PP7* transcription, i.e. the last time point at which *PP7* transcripts could be identified. 90% of nuclei with *PP7* activities contained single *PP7* activity traces. For the other 10% of nuclei in which there are two *PP7* activity traces, we aligned the initiation of the first trace or the termination of the second. There were cases where *eve-MS2* and *PP7* transcription started at the same time, presumably because *homie-homie* pairing occurred before *eve* enhancers started to function. Therefore, for the initiation analysis, we only aligned *PP7* activity traces where *eve-MS2* transcription appeared at least 3 min before *PP7* transcription was activated. Similarly, for the termination analysis, we only aligned *PP7* activity traces where *eve-MS2* transcription lasted for at least 3 min after *PP7* transcription ceased.

9. MSD analysis—We analyzed the relative motion between two associated spots (e.g. MS2 and parS) by computing the time-averaged mean squared displacement (MSD), i.e. the mean squared change in distances, between a specific spot pair over all time points separated by time interval Δt (Supplementary Fig. 4d). We computed an embryo-averaged MSD and a population-averaged MSD by pooling all spot pairs in an embryo and all spot pairs in a population of embryos, respectively. The embryo-averaged and population-averaged 3D MSDs were fit to a model for 3D anomalous diffusion, i.e. $MSD = 6D(\Delta t)^{\alpha}$ with an anomalous diffusion coefficient D and a scaling factor α that were extracted. Non-linear least-squares fits were performed for $\Delta t < 4$ min.

10. Classification of instantaneous topological states—Because of the fast chromatin motion ($D=0.04\ \mu m^2 s^{-0.24}$, Fig. 1e and Supplementary Fig. 4d) and the relatively small confinement of the enhancer-promoter locus (~1μm for the open state), distributions of the instantaneous E-P distance for the open state and the *homie-homie* paired state

overlapped significantly, which hindered the characterization of the instantaneous topological state of the enhancer-promoter locus. We therefore took advantage of the continuity of live imaging and calculated the velocity of the relative E-P movement (displacement across one frame) at each time point (Supplementary Fig. 8a, b). Since the time scale of topological state transitions seems to be at least one order of magnitude slower than the time resolution of our live imaging (which is validated by our kinetic model), the velocities provide extra information for identifying the instantaneous topological state.

We therefore used a binary classifier to classify each enhancer-promoter locus at each time point regarding its topological state, either open (O) or paired (P). We applied one training sample for each of the two states. For the open state, we used time series traces obtained from the *parS-λ-evePr-PP7* embryos, which presumably were composed solely of the open state. For the paired state, we used all traces where PP7 transcription occurred, considering that physical proximity is required for promoter activity so that time series traces accompanied by PP7 activity were exclusively in the paired state. For each training sample, we modeled the joint distribution of the distance vector and the velocity vectors as a multivariate Gaussian (Supplementary Fig. 8c-j). There is a negative correlation (-0.32, Pearson correlation coefficient) between velocities measured in two consecutive frames (Supplementary Fig. 8g-j), which is consistent with the strong sub-diffusive behavior we observed from the MSD analysis ($\alpha = 0.24$, Supplementary Fig. 4d).

Using the distance and the velocity information (Data), we calculated the likelihood p(Data|O-state) and p(Data|P-state) from the two trained joint distributions, respectively. Furthermore, we calculate the priors p(P-state) and p(O-state), for each developmental time point, by pooling data from all embryos. Specifically, we used a time window (5 min) centered at the specific time point and calculated the RMS distance for each nucleus. The distribution of these RMS distances was modeled as a two-component Gaussian mixture, and the proportion of the Gaussian component with the smaller mean was used as prior p(P-state) for this developmental time point.

The posterior probability p(P-state|Data) was then calculated according to Bayes rule. Finally, we estimated the errors (specificity and sensitivity) of our classifier from the two training samples, and a posterior probability cutoff that maximizes the Matthews correlation coefficient was used for state calling.

11. Modeling topological state transitions and MCMC Inference of kinetic parameters—We used a set of first-order reactions to model the transitions between the three topological states (Supplementary Fig. 9a). Based on the finding that physical proximity is required for transcriptional activation, we built a model such that P_{on} occurs only after P_{off} is established. Assuming that the parameters f_1 and b_1 are the same for both the *parS-homie-evePr-PP7* and the *parS-homie-noPr-PP7* constructs, we also used the O_{off} time series from the latter to constrain our parameter inference.

In order to infer the kinetic parameters, we used Metropolis-Hastings algorithm to perform MCMC. Specifically, given a parameter set:

$$\theta = \bigcup_{k = 1,2\ldots,8} \{\theta_k\} = \left\{f_1, b_1, f_2, b_2, b_3, F_{ini}\left(O_{off}, homie\right),\ F_{ini}\left(P_{on}, homie\right),\ F_{ini}\left(O_{off}, noPrmt\right)\right\}$$

where the three F_{ini} are the initial conditions for the indicated states and genotype, we used time series $D = \cup_{i,j}\left\{F_j(t_i), \sigma_j^2(t_i)\right\}$ to calculate likelihood:

$$P(D|\theta) = \prod_{i,j} N\left(f_j(t_i)|\theta,\ \mu_{i,j} = F_j(t_i), \sigma_j^2(t_i)\right)$$

where $f_j(t_i)\big|\theta$ is solved numerically from the coupled ODEs (Supplementary Fig. 9a) with MATLAB ode45. $F_{j=1,2,3}$ corresponds to the measured time series of the fraction of the O_{off} state for *parS-homie-evePr-PP7*, the fraction of the P_{on} state for *parS-homie-evePr-PP7* and the fraction of the O_{off} state for *parS-homie-noPr-PP7*, respectively, and $i = 1,2,\ldots,T$ are the developmental time points from 25 to 55 min in nuclear cycle 14.

Using prior $\pi_0(\theta) = \prod_k\left(1/\theta_k\right)$ and a log-normal proposal distribution:

$$J\left(\theta^*|\theta\right) = log\mathcal{N}(log(\theta), \sum)$$

we generated a Markov chain to sample posterior distributions of the kinetic parameters with acceptance probability:

$$\alpha\left(\theta^*, \theta\right) = \min\left(1,\ \frac{P\left(D|\theta^*\right)\pi_0\left(\theta^*\right)J\left(\theta|\theta^*\right)}{P(D|\theta)\pi_0(\theta)J\left(\theta^*|\theta\right)}\right) = \min\left(1,\ \prod_{i,j}\mathcal{N}\left(F_j(t_i)\middle|\theta^*, \sigma^2(t_i)\right)\prod_{i,j}\mathcal{N}\left(F_j(t_i)\middle|\theta, \sigma^2(t_i)\right)^{-1}\right)$$

All simulated chains converged after 5,000 iterations, and we used 90,000 stationary samples to represent the posterior distributions of the kinetic parameters (Supplementary Fig. 9c-g).

12. Transcriptional activity measurements—Transcriptional activity was measured as the sum of the pixel intensities in the spot mask (d = 1.4 μm, h = 2.3 μm). For aligned *PP7* activity traces (Fig. 2 and Supplementary Fig. 5) where *PP7* was not active (Red-OFF part), a mask around the parS spot (green) in the same nucleus was made. The mask was allowed to shift within the range defined by the mean parS-PP7 (green-red) distance. The maximal integrated intensity in the red channel was used as the *PP7* activity.

13. Endogenous *eve* activity comparison—For each trace with *PP7* activity, we integrated *eve-MS2* activity in the same nucleus to get *eve-MS2* activity while *PP7* transcription is active (eve|Red-ON, Fig. 4a, x-axis). Only nuclei with *PP7* activity lasting longer than 12 min were used. In order to obtain the control, which is the *eve-MS2* activity while PP7 transcription is not active (eve|Red-OFF, Fig. 4a, y-axis), we calculated the mean

of the integrated *eve-MS2* activities in the neighboring nuclei where *PP7* was not transcribed. Neighborhood is defined as nuclei within a 20μm anterior-posterior bin centered at the nucleus displaying *PP7* activity. The time interval for *eve-MS2* activity integration is the same as for the *PP7* expressing nucleus. The time-averaged integrated intensity is shown in Fig. 4a.

Statistical analysis

Two-tailed Wilcoxon rank sum tests were performed to compare E-P distances in different topological states. One-tailed Fisher's exact tests were performed to test for enhanced penetrance of the phenotypic defects associated with the *homie* transgenes. MCMC inference of the kinetics parameters is described in Image processing and data analysis. Representative images/videos were replicated in at least 3 independent experiments, as indicated in the relevant figure legends.

Data accessibility

Raw spot localization data is provided as Supplementary Dataset 1. Supplementary videos are provided as supplementary material 2 through 4.

Code availability

Custom codes (MATLAB) used for image processing and data analysis can be made available upon request. All details of algorithms are described in the Online Methods and references cited therein.

Supplementary Material

Refer to Web version on PubMed Central for supplementary material.

Acknowledgments

This study was funded by grants from the National Institutes of Health (U01 EB021239, U01 DA047730, R01 GM097275, R01 GM117458) and the National Science Foundation (PHY-1734030). H.C. was supported by the Charles H. Revson Biomedical Science Fellowship. M.L. was supported by the Rothschild, EMBO and HFSP fellowships.

References

1. Benoist C, Chambon P. In vivo sequence requirements of the SV40 early promotor region. Nature. 1981; 290:304–10. [PubMed: 6259538]
2. Levine M. Transcriptional enhancers in animal development and evolution. Curr Biol. 2010; 20:R754–63. [PubMed: 20833320]
3. Long HK, Prescott SL, Wysocka J. Ever-Changing Landscapes: Transcriptional Enhancers in Development and Evolution. Cell. 2016; 167:1170–1187. [PubMed: 27863239]
4. Buecker C, Wysocka J. Enhancers as information integration hubs in development: lessons from genomics. Trends Genet. 2012; 28:276–84. [PubMed: 22487374]
5. Kim TK, Shiekhattar R. Architectural and Functional Commonalities between Enhancers and Promoters. Cell. 2015; 162:948–59. [PubMed: 26317464]
6. Vernimmen D, Bickmore WA. The Hierarchy of Transcriptional Activation: From Enhancer to Promoter. Trends Genet. 2015; 31:696–708. [PubMed: 26599498]

7. Consortium, E.P. An integrated encyclopedia of DNA elements in the human genome. Nature. 2012; 489:57–74. [PubMed: 22955616]
8. Tolhuis B, Palstra RJ, Splinter E, Grosveld F, de Laat W. Looping and interaction between hypersensitive sites in the active beta-globin locus. Mol Cell. 2002; 10:1453–65. [PubMed: 12504019]
9. Uslu VV, et al. Long-range enhancers regulating Myc expression are required for normal facial morphogenesis. Nat Genet. 2014; 46:753–8. [PubMed: 24859337]
10. Zhang Y, et al. Chromatin connectivity maps reveal dynamic promoter-enhancer long-range associations. Nature. 2013; 504:306–10. [PubMed: 24213634]
11. Arnold CD, et al. Genome-wide quantitative enhancer activity maps identified by STARR-seq. Science. 2013; 339:1074–7. [PubMed: 23328393]
12. Ghavi-Helm Y, et al. Enhancer loops appear stable during development and are associated with paused polymerase. Nature. 2014; 512:96–100. [PubMed: 25043061]
13. Kvon EZ, et al. Genome-scale functional characterization of Drosophila developmental enhancers in vivo. Nature. 2014; 512:91–5. [PubMed: 24896182]
14. Levine M, Cattoglio C, Tjian R. Looping back to leap forward: transcription enters a new era. Cell. 2014; 157:13–25. [PubMed: 24679523]
15. Kagey MH, et al. Mediator and cohesin connect gene expression and chromatin architecture. Nature. 2010; 467:430–5. [PubMed: 20720539]
16. Mifsud B, et al. Mapping long-range promoter contacts in human cells with high-resolution capture Hi-C. Nat Genet. 2015; 47:598–606. [PubMed: 25938943]
17. Andrey G, et al. A switch between topological domains underlies HoxD genes collinearity in mouse limbs. Science. 2013; 340:1234167. [PubMed: 23744951]
18. Spitz F. Gene regulation at a distance: From remote enhancers to 3D regulatory ensembles. Semin Cell Dev Biol. 2016; 57:57–67. [PubMed: 27364700]
19. Carter D, Chakalova L, Osborne CS, Dai YF, Fraser P. Long-range chromatin regulatory interactions in vivo. Nat Genet. 2002; 32:623–6. [PubMed: 12426570]
20. Sanyal A, Lajoie BR, Jain G, Dekker J. The long-range interaction landscape of gene promoters. Nature. 2012; 489:109–13. [PubMed: 22955621]
21. Fujioka M, Wu X, Jaynes JB. A chromatin insulator mediates transgene homing and very long-range enhancer-promoter communication. Development. 2009; 136:3077–87. [PubMed: 19675129]
22. Fujioka M, Sun G, Jaynes JB. The Drosophila eve insulator Homie promotes eve expression and protects the adjacent gene from repression by polycomb spreading. PLoS Genet. 2013; 9:e1003883. [PubMed: 24204298]
23. Fujioka M, Mistry H, Schedl P, Jaynes JB. Determinants of Chromosome Architecture: Insulator Pairing in cis and in trans. PLoS Genet. 2016; 12:e1005889. [PubMed: 26910731]
24. Larson DR, Zenklusen D, Wu B, Chao JA, Singer RH. Real-time observation of transcription initiation and elongation on an endogenous yeast gene. Science. 2011; 332:475–8. [PubMed: 21512033]
25. Hocine S, Raymond P, Zenklusen D, Chao JA, Singer RH. Single-molecule analysis of gene expression using two-color RNA labeling in live yeast. Nat Methods. 2013; 10:119–21. [PubMed: 23263691]
26. Fukaya T, Lim B, Levine M. Enhancer Control of Transcriptional Bursting. Cell. 2016; 166:358–68. [PubMed: 27293191]
27. Dubarry N, Pasta F, Lane D. ParABS systems of the four replicons of Burkholderia cenocepacia: new chromosome centromeres confer partition specificity. J Bacteriol. 2006; 188:1489–96. [PubMed: 16452432]
28. Saad H, et al. DNA dynamics during early double-strand break processing revealed by non-intrusive imaging of living cells. PLoS Genet. 2014; 10:e1004187. [PubMed: 24625580]
29. Gasser SM. Visualizing chromatin dynamics in interphase nuclei. Science. 2002; 296:1412–6. [PubMed: 12029120]

30. Sinclair P, Bian Q, Plutz M, Heard E, Belmont AS. Dynamic plasticity of large-scale chromatin structure revealed by self-assembly of engineered chromosome regions. J Cell Biol. 2010; 190:761–76. [PubMed: 20819934]
31. Bystricky K. Chromosome dynamics and folding in eukaryotes: Insights from live cell microscopy. FEBS Lett. 2015; 589:3014–22. [PubMed: 26188544]
32. Garcia HG, Tikhonov M, Lin A, Gregor T. Quantitative imaging of transcription in living Drosophila embryos links polymerase activity to patterning. Curr Biol. 2013; 23:2140–5. [PubMed: 24139738]
33. Fukaya T, Lim B, Levine M. Rapid Rates of Pol II Elongation in the Drosophila Embryo. Curr Biol. 2017; 27:1387–1391. [PubMed: 28457866]
34. Lucas JS, Zhang Y, Dudko OK, Murre C. 3D trajectories adopted by coding and regulatory DNA elements: first-passage times for genomic interactions. Cell. 2014; 158:339–52. [PubMed: 24998931]
35. Guo Y, et al. CRISPR Inversion of CTCF Sites Alters Genome Topology and Enhancer/Promoter Function. Cell. 2015; 162:900–10. [PubMed: 26276636]
36. Rao SS, et al. A 3D map of the human genome at kilobase resolution reveals principles of chromatin looping. Cell. 2014; 159:1665–80. [PubMed: 25497547]
37. Deng W, et al. Reactivation of developmentally silenced globin genes by forced chromatin looping. Cell. 2014; 158:849–60. [PubMed: 25126789]
38. Franke M, et al. Formation of new chromatin domains determines pathogenicity of genomic duplications. Nature. 2016; 538:265–269. [PubMed: 27706140]
39. Dixon JR, et al. Chromatin architecture reorganization during stem cell differentiation. Nature. 2015; 518:331–6. [PubMed: 25693564]
40. Krijger PH, et al. Cell-of-Origin-Specific 3D Genome Structure Acquired during Somatic Cell Reprogramming. Cell Stem Cell. 2016; 18:597–610. [PubMed: 26971819]
41. Raser JM, O'Shea EK. Control of stochasticity in eukaryotic gene expression. Science. 2004; 304:1811–4. [PubMed: 15166317]
42. Voss TC, Hager GL. Dynamic regulation of transcriptional states by chromatin and transcription factors. Nat Rev Genet. 2014; 15:69–81. [PubMed: 24342920]
43. Sanchez A, Garcia HG, Jones D, Phillips R, Kondev J. Effect of promoter architecture on the cell-to-cell variability in gene expression. PLoS Comput Biol. 2011; 7:e1001100. [PubMed: 21390269]
44. Hug CB, Grimaldi AG, Kruse K, Vaquerizas JM. Chromatin Architecture Emerges during Zygotic Genome Activation Independent of Transcription. Cell. 2017; 169:216–228.e19. [PubMed: 28388407]
45. Rubin AJ, et al. Lineage-specific dynamic and pre-established enhancer-promoter contacts cooperate in terminal differentiation. Nat Genet. 2017
46. Hnisz D, Shrinivas K, Young RA, Chakraborty AK, Sharp PA. A Phase Separation Model for Transcriptional Control. Cell. 2017; 169:13–23. [PubMed: 28340338]
47. Sexton T, Umlauf D, Kurukuti S, Fraser P. The role of transcription factories in large-scale structure and dynamics of interphase chromatin. Semin Cell Dev Biol. 2007; 18:691–7. [PubMed: 17950637]
48. Cho WK, et al. RNA Polymerase II cluster dynamics predict mRNA output in living cells. Elife. 2016; 5
49. Williamson I, Lettice LA, Hill RE, Bickmore WA. Shh and ZRS enhancer colocalisation is specific to the zone of polarising activity. Development. 2016; 143:2994–3001. [PubMed: 27402708]
50. Stadler MR, Haines JE, Eisen MB. Convergence of topological domain boundaries, insulators, and polytene interbands revealed by high-resolution mapping of chromatin contacts in the early Drosophila melanogaster embryo. Elife. 2017; 6
51. Negre N, et al. A comprehensive map of insulator elements for the Drosophila genome. PLoS Genet. 2010; 6:e1000814. [PubMed: 20084099]
52. Kyrchanova O, Georgiev P. Chromatin insulators and long-distance interactions in Drosophila. FEBS Lett. 2014; 588:8–14. [PubMed: 24211836]

53. Chetverina D, et al. Boundaries of loop domains (insulators): Determinants of chromosome form and function in multicellular eukaryotes. Bioessays. 2017; 39
54. Lupianez DG, et al. Disruptions of topological chromatin domains cause pathogenic rewiring of gene-enhancer interactions. Cell. 2015; 161:1012–25. [PubMed: 25959774]
55. Bartman CR, Hsu SC, Hsiung CC, Raj A, Blobel GA. Enhancer Regulation of Transcriptional Bursting Parameters Revealed by Forced Chromatin Looping. Mol Cell. 2016; 62:237–47. [PubMed: 27067601]
56. Wu B, Chen J, Singer RH. Background free imaging of single mRNAs in live cells using split fluorescent proteins. Sci Rep. 2014; 4:3615. [PubMed: 24402470]
57. Sladitschek HL, Neveu PA. MXS-Chaining: A Highly Efficient Cloning Platform for Imaging and Flow Cytometry Approaches in Mammalian Systems. PLoS One. 2015; 10:e0124958. [PubMed: 25909630]
58. Vodala S, Abruzzi KC, Rosbash M. The nuclear exosome and adenylation regulate posttranscriptional tethering of yeast GAL genes to the nuclear periphery. Mol Cell. 2008; 31:104–13. [PubMed: 18614049]
59. Dubarry M, Loiodice I, Chen CL, Thermes C, Taddei A. Tight protein-DNA interactions favor gene silencing. Genes Dev. 2011; 25:1365–70. [PubMed: 21724830]
60. Bateman JR, Lee AM, Wu CT. Site-specific transformation of Drosophila via phiC31 integrase-mediated cassette exchange. Genetics. 2006; 173:769–77. [PubMed: 16547094]
61. Small S. In vivo analysis of lacZ fusion genes in transgenic Drosophila melanogaster. Methods Enzymol. 2000; 326:146–59. [PubMed: 11036640]
62. Little SC, Tkacik G, Kneeland TB, Wieschaus EF, Gregor T. The formation of the Bicoid morphogen gradient requires protein movement from anteriorly localized mRNA. PLoS Biol. 2011; 9:e1000596. [PubMed: 21390295]
63. Little SC, Tikhonov M, Gregor T. Precise developmental gene expression arises from globally stochastic transcriptional activity. Cell. 2013; 154:789–800. [PubMed: 23953111]
64. Dubuis JO, Samanta R, Gregor T. Accurate measurements of dynamics and reproducibility in small genetic networks. Mol Syst Biol. 2013; 9:639. [PubMed: 23340845]
65. Gao Y, Kilfoil ML. Accurate detection and complete tracking of large populations of features in three dimensions. Opt Express. 2009; 17:4685–704. [PubMed: 19293898]
66. Dijkstra EW. A note on two problems in connexion with graphs. Numer Math. 1959; 1:269–271.

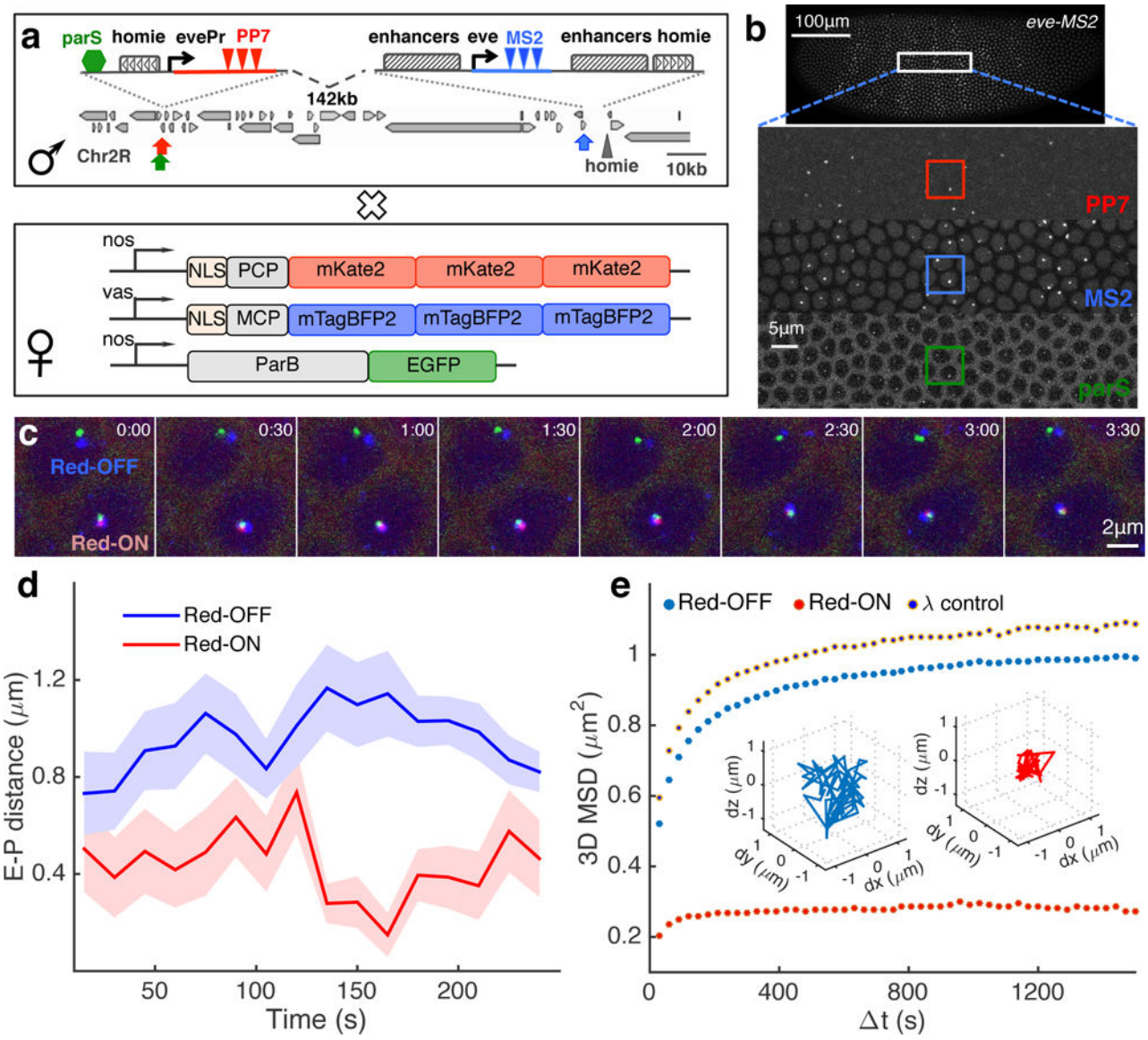

Figure 1. Three-color live imaging of enhancer-promoter movement and transcriptional activity

a, Male flies carrying the modified *eve* locus are crossed with females carrying maternally expressed blue, red and green fluorescent proteins that are fused to MS2 coat protein (MCP), PP7 coat protein (PCP) and ParB DNA binding protein, respectively. In the male flies, a reporter with an *eve* promoter (*evePr*) driving *PP7* transcription is integrated at −142 kb upstream of an MS2-tagged endogenous *eve* locus in the *Drosophila* genome. An ectopic *homie* insulator sequence is also included in the reporter in order to force loop formation through *homie-homie* pairing. Furthermore, a *parS* sequence is integrated near the *homie-evePr-PP7* reporter. **b**, Snapshot of a representative embryo generated from crosses shown in **a**. The embryo displays fluorescent foci for MS2, PP7 and parS in the corresponding channels. **c**, 8 snapshots of a time course following two nuclei for ~4 min. The lower nucleus displays *PP7* activity (Red-ON), the upper has none (Red-OFF). **d**, Instantaneous physical enhancer–promoter (E-P) distance between endogenous *eve* enhancers (blue signal) and the

PP7 reporter (green signal) as a function of time for the Red-OFF and Red-ON nuclei in **c**. Error bar corresponds to measurement error estimated from the co-localization control experiments (see Supplementary Fig. 3). **e**, Population-averaged MSD calculated from E-P distance trajectories obtained from all Red-ON (n=720) and Red-OFF (n=7,163) nuclei, as well as for a control construct where *homie* in the reporter is replaced by phage λ DNA (λ control, n=1,453). Inset shows two representative trajectories for a Red-OFF nucleus (blue) and a Red-ON (red) nucleus, respectively.

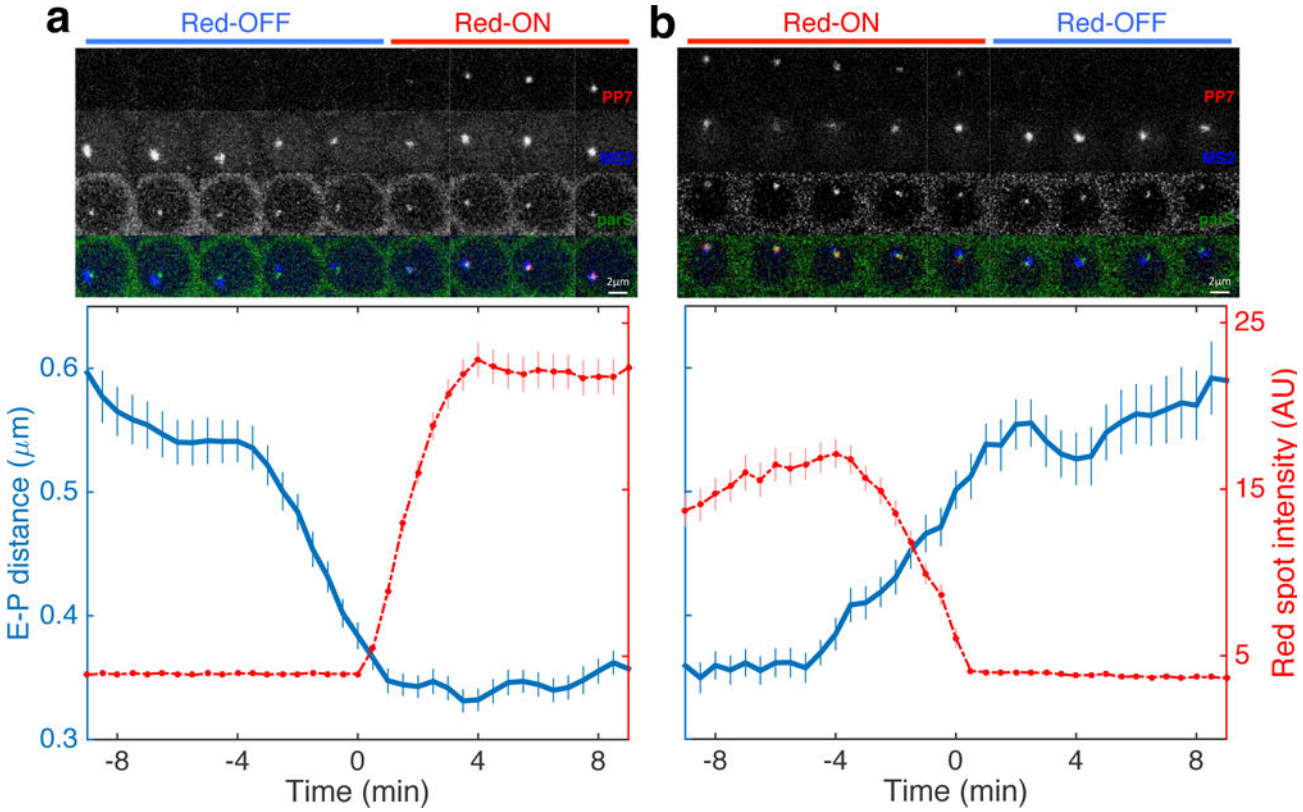

Figure 2. Sustained physical enhancer–promoter proximity is necessary for productive transcription

a, Average transcription activity (red) and E-P distance (RMS distance between blue and green foci) as a function of time for 286 nuclei transitioning from the Red-OFF to Red-ON state. Time series for individual nuclei are aligned such that *PP7* activity starts at 0 min, i.e. first occurrence of red signal. Top panel shows a series of raw images of a representative nucleus that transitions from Red-OFF to Red-ON (see also Supplementary Video 4). **b**, Average transcription activity and E-P distance as a function of time for 203 nuclei transitioning from Red-ON to Red-OFF. Time series for individual nuclei are aligned such that *PP7* activity ends at 0 min, i.e. disappearance of red signal. The top panel shows a series of raw images of a representative nucleus that transitions from Red-ON to Red-OFF (see also Supplementary Video 4). All error bars are standard errors of the mean.

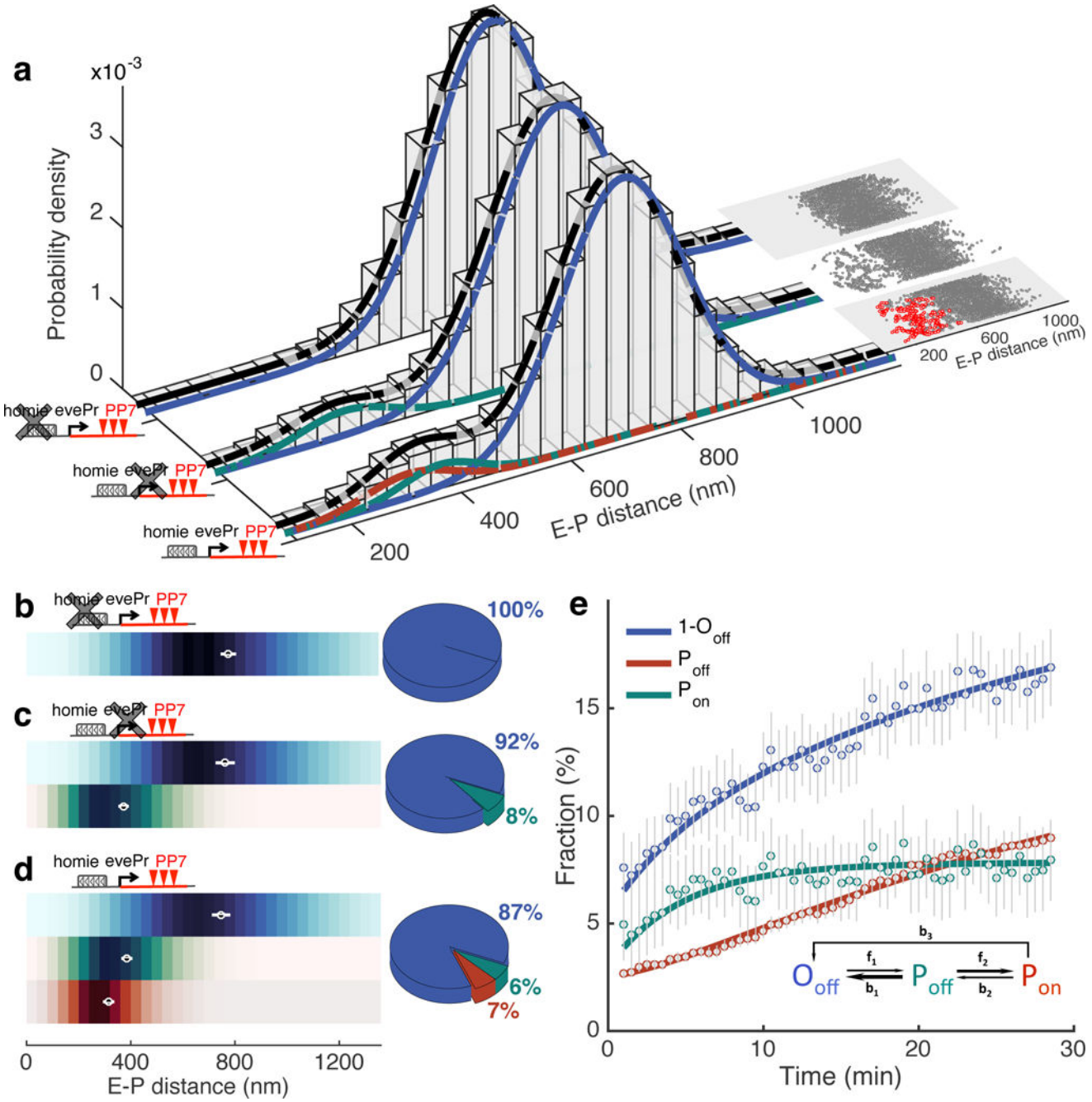

Figure 3. Characterization of topological enhancer-promoter conformations, the kinetic transitions between them, and their relation to transcriptional activation

a, E-P distance distribution for three experimental constructs: *parS-homie-evePr-PP7* (n=265,277 RMS E-P distances from 7,883 trajectories in 84 embryos), *parS-homie-noPr-PP7* (n=81,629 RMS E-P distances from 2,566 trajectories in 29 embryos) and *parS-λ-evePr-PP7* (n=49,587 RMS E-P distances from 1,453 trajectories in 15 embryos). A 5-min sliding window along each time trace is used to calculate RMS E-P distances. Gaussian mixture models for all RMS samples are shown with black curves for each construct. Gaussian mixture models for RMS samples in which PP7 is not active are shown with blue

(larger mean) and green (smaller mean) curves. Red curve is Gaussian fitting for all RMS distance samples accompanied by continuous PP7 transcription. Insets show scatter plots of RMS distance from one representative embryo for each construct. Each data point is a time-averaged RMS distance. Red points indicate continuous PP7 transcription across the window. **b-d**, Distribution of instantaneous E-P distance for E-P topological states classified as O_{off} (blue), P_{off} (green) or P_{on} (red) for *parS-λ-evePr-PP7* (**b**), *parS-homie-noPr-PP7* (**c**) and *parS-homie-evePr-PP7* (**d**). Means±STD of RMS distance calculated from individual embryos shown as white circles with bars. Adjacent pie charts show the fraction of each E-P topological state. See also Supplementary Fig. 8. **e**, Fraction of each topological state for the *parS-homie-evePr-PP7* construct as a function of developmental time, starting 25 min into nc14. Error bars are bootstrapped standard errors of state fractions. Solid lines are fits derived from kinetic parameters obtained from MCMC (Markov Chain Monte Carlo) inference. Inset shows the kinetic model capturing the transitions between the three topological states; arrow widths represent transition time scales (wider arrows correspond to faster rates, see Supplementary Fig. 9 for values).

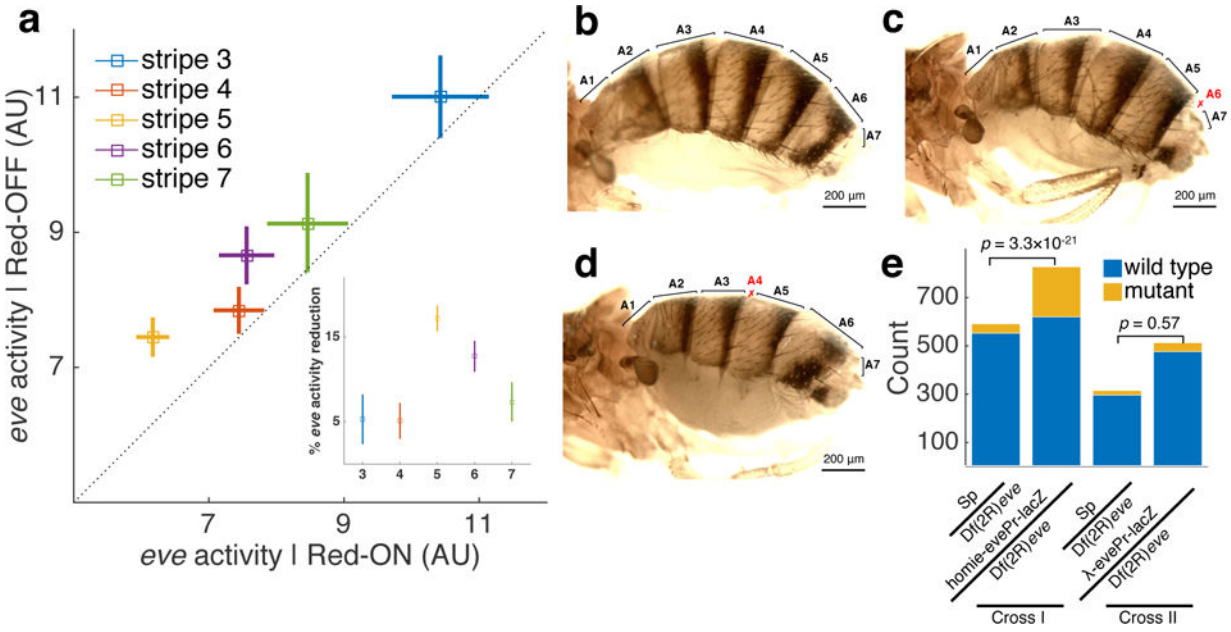

Figure 4. Long-distance-mediated promoter competition results in patterning phenotypes

a, Endogenous *eve-MS2* activity in nuclei that also display *PP7* reporter activity (x-axis) is lower than in the neighboring nuclei where *PP7* is not expressed (y-axis). Means±SEMs (n=45, 106, 143, 85 and 27 *PP7* expressing nuclei for stripe 3-7, respectively). Inset: Reduction in *eve-MS2* activity for each stripe. Error bars are bootstrapped standard errors of the percentage reduction. **b-d**, Adult wild-type (**b**) and mutant (**c**, **d**) flies from crosses between *Sp*/*homie-evePr-lacZ* males and *CyO*/*Df*(2R)*eve*$^{-}$ females. c and d show defects in abdominal segments A4 and A6, respectively, resulting from reduced *eve* activity in stripe 5 and stripe 6, respectively. Abdominal segments are labeled, with defective segments marked in red. **e**, Results of phenotype scoring. Mutant counts include both A4 and A6 phenotypes. Cross I: single *Sp*/*homie-evePr-lacZ* males were crossed with *CyO*/*Df*(2R)*eve*$^{-}$ females, and scoring results from 47 individual vials were summed. Cross II: single *Sp*/*λ-evePr-lacZ* males were crossed with *CyO*/*Df*(2R)*eve*$^{-}$ females, and results from 23 individual vials were summed. P-values are from one-tailed Fisher's exact test.